Automatic SWI Venography Segmentation Using Conditional Random Fields

Silvain Bériault*, Yiming Xiao, *Student Member, IEEE*, D. Louis Collins, and G. Bruce Pike, *Senior Member, IEEE*

***Abstract*—Susceptibility-weighted imaging (SWI) venography can produce detailed venous contrast and complement arterial dominated MR angiography (MRA) techniques. However, these dense reversed-contrast SWI venograms pose new segmentation challenges. We present an automatic method for whole-brain venous blood segmentation in SWI using Conditional Random Fields (CRF). The CRF model combines different first and second order potentials. First-order association potentials are modeled as the composite of an appearance potential, a Hessian-based shape potential and a non-linear location potential. Second-order interaction potentials are modeled using an auto-logistic (smoothing) potential and a data-dependent (edge) potential. Minimal post-processing is used for excluding voxels outside the brain parenchyma and visualizing the surface vessels. The CRF model is trained and validated using 30 SWI venograms acquired within a population of deep brain stimulation (DBS) patients (age range = 43-73 years). Results demonstrate robust and consistent segmentation in deep and sub-cortical regions (median kappa = 0.84 and 0.82), as well as in challenging mid-sagittal and surface regions (median kappa = 0.81 and 0.83) regions. Overall, this CRF model produces high-quality segmentation of SWI venous vasculature that finds applications in DBS for minimizing hemorrhagic risks and other surgical and non-surgical applications.**

***Index Terms*—Conditional random fields, deep brain stimulation, image-guided neurosurgery, MR venography, susceptibility-weighted imaging.**

I. Introduction

EFFECTIVE visualization and modeling of the cerebral vasculature is extremely valuable for planning a variety of image-guided neurosurgical procedure such as identifying vessel-free path for insertion of a biopsy needle or implantation of Deep Brain Stimulation (DBS) probes or stereotaxic electro encephalography electrodes. However, 3D cerebrovascular models used clinically are generally incomplete due to the extent of labor required to segment the vasculature and because the vascular contrast in conventional MR angiography (MRA) protocols that involve injection of gadolinium decreases rapidly with vessel size.

Susceptibility-weighted imaging (SWI) venography [1], [2] is a recent technique that exploits both the magnitude and phase of complex T2*-weighted MRI signal to increase sensitivity to deoxygenated (venous) blood. This protocol can image cerebral veins with superior contrast and has been shown to improve selection of DBS plans that avoid finer sub-cortical and deep veins not visible on standard gadolinium contrast [3]. However, SWI poses new segmentation challenges, because it produces dense venograms that cannot be segmented using manual or semi-automatic methods within a reasonable time, and because SWI is also sensitive to iron-rich brain structures and to signal loss at inter-hemispheric fissure and air-tissue interfaces. Separation of surface veins and skull is also challenging because both structures are hypointense.

The choice of an optimal segmentation strategy depends upon several factors including the targeted application [4]. For pre-surgical planning applications, the most influential factors are: i) robustness to variable image quality, ii) completeness of segmentation and iii) automation level. Less important factors are computational efficiency (preoperative images are often acquired the day before surgery) and vessel contour accuracy (as it would be in vessel quantification studies).

A. Previous Work

Different methods for automatic vessel segmentation methods have been proposed in the computer vision literature. We briefly review three main classes of techniques for vessel enhancement and segmentation—statistical methods, scale-space methods, and deformable models—with special emphasis on cerebrovascular (whole-brain) applications. More complete reviews are available in [4], [5].

Statistical methods make hypotheses about vessel appearance relative to other tissues. Different appearance models were proposed for time-of-flight (TOF) MRA [6]–[9], phase contrast (PC) MRA [10], and CT-angiography (CTA) [11]. These models estimate intensity distributions for vessels and other tissues, often by fitting a Finite Mixture Model (FMM) to the dataset's histogram. Discrete segmentation is then computed via independent (voxel-by-voxel) classification or Markov Random Field (MRF) (see Section II).

Scale-space methods make geometric assumptions about the shape of vessels (e.g., elongation, tubularity). Several multiscale vessel enhancement filters (e.g., [12]–[15]) were defined based on principal eigenvalue conditions of the MRI intensity Hessian matrix that characterize local tubularity (i.e., $\lambda_1 \approx 0, \lambda_2 \approx \lambda_3 \gg \lambda_1$). Alternatively, spherical flux filters [16],

Manuscript received March 10, 2015; revised May 14, 2015; accepted May 20, 2015. Date of publication June 05, 2015; date of current version November 25, 2015. *Asterisk indicates corresponding author.*

*S. Bériault is with the McConnell Brain Imaging Centre, Montreal Neurological Institute, McGill University, Montreal, QC, H3A 2B4 Canada (e-mail: silvain.beriault@mail.mcgill.ca).

Y. Xiao and D. L. Collins are with the McConnell Brain Imaging Centre, Montreal Neurological Institute, McGill University, Montreal, QC, H3A 2B4 Canada.

G. B. Pike is with the Hotchkiss Brain Institute, University of Calgary, Calgary, AB, T2N 1N4 Canada (e-mail: bruce.pike@ucalgary.ca).

Color versions of one or more of the figures in this paper are available online at http://ieeexplore.ieee.org.

Digital Object Identifier 10.1109/TMI.2015.2442236

[17] enhance vasculature by computing the outward flux of a gradient vector field for spheres of increasing radius. Law and Chung [18] extended this approach to exploit vessel directionality via an optimal gradient projection axis.

Deformable models make the assumption that vessels are connected, and evolve an initial seed surface placed inside the vascular tree until it fills the whole tree. Implementations that use a level-set formulation [19] are often preferred because they implicitly model topological changes. Different deformable models were proposed and validated on PC MRA [17], [20] and TOF MRA [16], [21].

Shape-based techniques are particularly robust for enhancing vessels in low-contrast areas and have been used for enhancing SWI venography [22]–[26]. However, these filters make strong geometric assumptions that can under-segment surface veins, especially in reversed-contrast SWI, and vascular anomalies (e.g., large aneurysms). Non-parametric (appearance-based) techniques in SWI find limitations in brain areas sensitive to susceptibility-induced signal loss (e.g., in the mid-sagittal plane, or basal ganglia). Deformable models come with the challenge of defining a speed term that allows surface evolution into all branches (including smaller low-contrast branches) without leaking into non-vessel structures elsewhere [21]. Also, incomplete contrast in SWI can break the connectedness assumption posed by the technique.

B. Our Approach

This work presents a new Conditional Random Field (CRF) for segmenting SWI venography datasets. The CRF model aggregates multiple first- and second-order potentials. Specifically, appearance, shape, location, auto-logistic (Ising) interaction and data-dependent interaction potentials are combined to produce robust, complete and fully automated SWI venogram segmentation. Our method is validated on a database of 30 SWI datasets acquired from a population of elderly DBS/Parkinson's patients.

The rest of the paper is organized as follows. Section II reviews the fundamentals of MRF/CRF modeling and inference. Section III elaborates on the design of a new CRF model for segmenting SWI venography datasets. Section IV describes the experimental methodology used for estimating optimal CRF parameters and validating the CRF segmentation performance. Section V presents quantitative and qualitative SWI segmentation results. Finally, Section VI summarizes the main findings and provides some insights about potential future works.

II. Background

The segmentation of cerebral veins from raw SWI data can be defined as a labeling problem. The goal is to assign a discrete label $l \in \{V, T\}$ to each voxel based on observed MRI data $Y = \{y_0, \ldots, y_i, \ldots y_{N-1}\}$. This labeling process results in a discrete dataset $X = \{x_0, \ldots, x_i, \ldots, x_{N-1}\}$ where each voxel x_i inside the brain parenchyma is classified either as vessel (V) or other tissue (T).

Many statistical classifiers infer the posterior distribution $P(X|Y)$ of the labels given the observations using an independent scheme that segment each x_i based on a single observation y_i, without taking into consideration the spatial coherence between neighboring classifications. These independent methods are thus limited due to noise in the data and possible intensity overlap between the different classes. Markov Radom Field (MRF) methods can overcome these limitations.

In MRF theory, the classification X is modeled as a random process that obeys a Gibbs distribution of the form: $P(X) = Z^{-1}\exp(-U(X))$. $U(X)$ is an energy function that models the spatial interaction between the labels in X. $Z = \sum \exp(-U(X))$ is a normalizing constant that sums all possible configurations of X. Upon modeling $U(X)$, optimal classification X^* is obtained by maximizing $P(X|Y) \propto P(Y|X)P(X)$.

A. MRF/CRF Modeling

A fundamental challenge in MRF-based segmentation is to model an energy function for which the desired labeling X^* is the minimum of $U(X)$. For segmentation application, it is common to limit the model to pair-wise voxel interactions [27] and to pose a smoothness assumption about the desired labeling X^*. As such, the auto-logistic MRF model (or Ising-MRF in binary cases) has been extensively used for regularizing statistical FMM classification. Such MRF can be described as:

$$P(X|Y) = \frac{1}{Z}\exp\left(\sum_{i\in S}\log(p(y_i|x_i)) + \sum_{i\in S}\sum_{j\in\eta_i} -\beta(1-\delta(x_i - x_j))\right). \quad (1)$$

The left summation is computed over all voxels. $p(y_i|x_i)$ is a likelihood probability that is generally estimated via some low-level FMM process. The right summation is computed over all pairs of neighboring voxels (η_i denotes all voxels j within a local neighborhood of voxel i). β is a fixed penalty for each occurrence of $x_i \neq x_j$. This MRF formulation provides a useful framework for smoothing the segmentation output but can also erase vessels with a diameter smaller than the size of η_i as previously reported [7], [24]. This effect can be partially mitigated with asymmetric penalty terms [28], with different configurations of local neighborhood [9], or, as investigated in this study, with data-dependent interactions.

Conditional random fields (CRF) extend conventional MRFs by unrestricting the use of all observations Y to describe first and high-order potentials. In the most general form, a CRF can be formulated as:

$$P(X|Y) = \frac{1}{Z}\exp\left(\sum_{i\in S} V_1(x_i|Y) + \sum_{i\in S}\sum_{j\in\eta_i} V_2(x_i, x_j|Y)\right). \quad (2)$$

Similarly to (1), V_1 is a first-order "association" potential and V_2 a second-order interaction potential. However, both V_1 and V_2 can depend on parts or all observations in Y. One common application of CRFs is to reduce the strength of V_2 interactions when the local observations indicate the presence of an edge in the data. Data-dependent interaction provides superior capabilities for segmenting fine structures, such as small white-matter lesions [29], [30] or CTA vasculature [11].

B. MRF/CRF Inference

A number of local and global optimization methods exist to estimate X^*. In particular, Iterated Conditional Modes (ICM) [31] and Graph Cuts [32], [33] are two well-known methods for MRF/CRF inference. Other methods exist but they are not as widely used for cerebrovascular segmentation. The reader is referred to [27] for an overview of different MRF/CRF solvers.

ICM is a greedy method that minimizes $U(X)$ locally at each site x_i iteratively until convergence. ICM is generally fast to converge. However, one disadvantage with the method is that it is sensitive to initialization with a pre-segmentation that is close to the optimal solution X^*. An independent classification of first-order potentials (V_1 only) is generally sufficient as a pre-segmentation. Hassouna *et al.* [7] and Zhou *et al.* [9] both used ICM to segment time-of-flight MRA of the brain.

Alternatively, Graph Cuts is a popular global optimization method for solving discrete MRF/CRF. The main advantage of Graph Cuts is that it can find a globally optimal solution in polynomial time for binary segmentation cases. However, one main limitation with standard Graph Cuts technique is that it only applies to a subset of MRF/CRF with sub-modular energy (i.e., $V_2(V,T) + V_2(T,V) > V_2(V,V) + V_2(T,T)$). This constraint puts important limitations on the MRF/CRF model that are not posed by ICM or other local optimizers. Furthermore, there is a potential shrinking bias due to the estimation of a minimum cut that must be taken into account since the structure of interest in SWI consists of many thin vessel branches.

III. Method

The proposed SWI-CRF segmentation builds upon (2). Specifically, it aggregates multiple first-order association potentials and second-order interaction potentials (see Sections III-A and III-B), which are then used to estimate classification X^* (see Section III-C). Minimal post-processing is used to exclude hypointense voxels outside the brain parenchyma thereby enabling visualization of surface veins (see Section III-D).

A. Association Potential

Similarly to [30], the association potential is defined as the composite of three potentials: appearance (φ), shape (ψ) and location (ϕ):

$$V_1(x_i|Y) = \log\left(\varphi(x_i|Y_\varphi)\right) + \log\left(\psi(x_i|Y_\psi)\right) + \log\left(\phi(x_i|Y_\phi)\right). \quad (3)$$

The association potential $V_1(x_i|Y)$ classifies each voxel i independently from the classification of neighboring voxels. The classification is thus based solely on the observations Y or a subset of observations. In (3), Y_φ, Y_ψ and Y_ϕ are subsets of Y used respectively for computation of appearance, shape and location potentials.

The appearance potential $\varphi(x_i|Y_\varphi)$ models cerebral vasculature with the underlying assumption that venous blood is hypointense relatively to other tissues in SWI. The appearance potential is implemented as a FMM. Thus, Y_φ is simply the observation y_i. The shape potential $\psi(x_i|Y_\psi)$ incorporates local tubularity constraints into the segmentation. The shape potential is implemented using a Hessian-based vesselness measure. Thus, Y_ψ is a local subset of Y used for calculation of the local vesselness ($\mathcal{V}_i$). The location potential $\phi(x_i|Y_\phi)$ incorporates prior atlas information about the expected location of vessels and other tissues within the brain. Thus, Y_ϕ is the full dataset since all observations are needed for calculating a transformation that maps the voxels to atlas locations.

All association potentials are defined on a [0-1] range and combined in a multiplicative way or, as per (3), by summing their $\log(\cdot)$. The relative importance of each potential is implicit to the implementation (and fuzziness) of the potential functions $\varphi(\cdot)$, $\psi(\cdot)$, and $\phi(\cdot)$ as described next. Rather than using fixed weights for the different potentials, this CRF is configured such that the shape and location potentials are most active in brain regions where appearance cannot discriminate between vessel and tissue and less active otherwise.

1) Appearance Potential: The appearance potential models dependencies between the labels X and the raw observations Y_φ (i.e., the intensities). Similarly to other statistical vessel segmentation protocols, we used a FMM to model likelihood distributions $p(y_i|x_i)$ for each label, but with the reverse assumption that vessels are hypointense. The appearance potential is thus described as:

$$\varphi(x_i|Y_\varphi) = p(y_i|x_i). \quad (4)$$

The hypointense vessel class is modeled as one normal distribution. The tissue class in SWI aggregates different brain structures with low (e.g., iron), medium (eg. the ventricles) and high (e.g., white-matter, grey-matter) intensities, and is modeled as a mixture of three normal distributions. The total probability density function of the FMM is described as:

$$p(y_i) = \sum_{k=0}^{3} w_k p(y_i|k) \quad (5)$$

w_k is the class proportion and $p(y_i|k) \sim \mathcal{N}(\mu_k, \sigma_k)$. The FMM parameters $\theta = \{w_k, \mu_k, \sigma_k\}$, are estimated by Expectation-Maximization [34]. Following EM parameter estimation, likelihoods for V and T classes are:

$$\begin{aligned} p(y_i|x_i = V) &= \mathcal{N}(\mu_0, \sigma_0) \\ p(y_i|x_i = T) &= \frac{\sum_{k=1..3} w_k \mathcal{N}(\mu_k, \sigma_k)}{w_1 + w_2 + w_3}. \end{aligned} \quad (6)$$

The first and second columns of Fig. 1 respectively show a raw SWI dataset in different regions of the brain and the computed appearance potentials (vessel class). While the appearance potential is appropriate to describe vasculature at the brain surface and sub-cortically, other sources of signal-loss can perturb the segmentation within basal ganglia or at the mid-sagittal plane (see red arrows in Fig. 1).

2) Shape Potential: The shape potential complements the appearance potential by favoring the V class for voxels that are locally tubular and otherwise penalizing voxels that deviate from this assumption. Specifically, the shape potential is modeled as:

$$\psi(x_i = V|Y_\psi) = \sigma(\mathcal{V}_i). \quad (7)$$

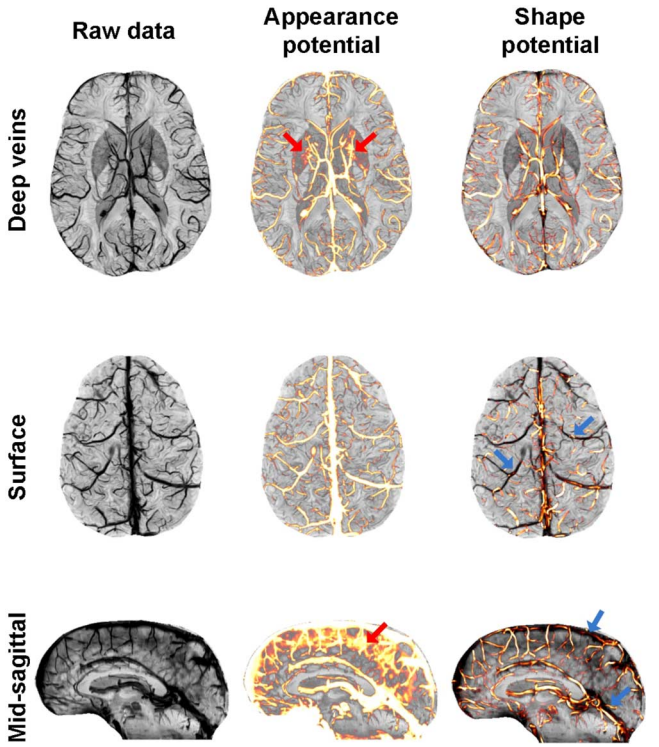

Fig. 1. Appearance and Hessian-based shape potentials. The appearance potential is sensitive to any hypointense structure including the vasculature, but also iron-rich lenticular nuclei and signal-loss at the inter-hemispheric fissure (see red arrows). The shape potential detects vasculature as local tubularity in the data but can under-segment surface vasculature and large sinuses in mid-sagittal plane (see blue arrows).

$\mathcal{V}_i$ is Frangi *et al.*'s [14] maximal vesselness response at voxel i. $\sigma(\cdot)$ is a sigmoid function of the form $\sigma(x) = 1/(1+e^{-a_i(x+b)})$. Parameter b moves $\sigma(\cdot)$ to an appropriate decision threshold. Parameter a_i controls the fuzziness of the $\sigma(\cdot)$ at voxel i. As illustrated in Fig. 1 (third column), Hessian-based filtering can detect tubular vessels even in low-contrast regions. However, it is also an imperfect descriptor of the SWI vasculature, especially at the brain surface. Therefore, a_i is weighted according to the local risk (r^{leak}) that the appearance potential leaks into other hypointense structures. Thus, we have:

$$a_i = a \cdot r_i^{leak} \tag{8}$$

with

$$r_i^{leak} = \max\left\{\frac{1}{(\|D_i\|+1)}, \mathcal{O}_i\mathcal{M}_i\right\} \cdot \left(1 - p(x_i|Y_\phi, \mathcal{A}^{sinuses})\right). \tag{9}$$

$\|D_i\|$ is the Euclidean distance to the midline in stereotactic space. $\mathcal{O}_i$ is a generalized Hessian-based objectness measure [35], that extends the vesselness measure to be sensitive to large plate-like hypointense structures (see Fig. 2 for an example). $\mathcal{M}_i$ is a binary brain mask that disables $\mathcal{O}_i$ at the brain surface. $p\left(x_i|Y_\phi, \mathcal{A}_i^{sinuses}\right)$ is an atlas probability of vessel presence (see next section). a is a global factor to be estimated. Overall, the shape potential is most active near the midline and within large hypointense patches detected by the $\mathcal{O}_i$ measure.

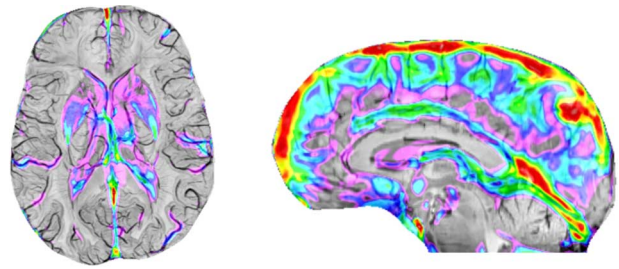

Fig. 2. Modified Hessian analysis to detect large hypointense plates. This is an anti-pattern to identify low-contrast brain regions where an appearance-only potential may fail.

Reciprocally, the shape potential is less active at the brain surface, within sub-cortical regions and at atlas locations with high-probability of vessel presence.

3) Location Potential: The location potential further guides the segmentation by incorporating three probabilistic atlas $\left(\mathcal{A}^{BG}, \mathcal{A}^{sinuses}, \mathcal{A}^{skin}\right)$ as follows:

$$\phi(x_i = V|Y_\phi) = \max\left\{\begin{array}{c} p(x_i|Y_\phi, \mathcal{A}^{sinuses}), \\ p(x_i|Y_\phi, \mathcal{A}^{skin}), \\ 0.05 \end{array}\right\} \cdot \left(1 - p(x_i|Y_\phi, \mathcal{A}^{BG})\right) \tag{10}$$

$p(x_i|Y_\phi, \mathcal{A})$ represents a [0-1] probabilistic value for a given atlas $(\mathcal{A})$ at voxel x_i after non-linear deformation to the patient data (Y_ϕ). $\mathcal{A}^{sinuses}$ is an atlas that predicts the location of large veins that have low inter-subject variability such as the superior sagittal sinus and the straight sinus. These veins are challenging to segment on SWI because they receive less signal attenuation in comparison to smaller veins[1]. $\mathcal{A}^{skin}$ is a skin atlas that prevents hyperintense non-parenchyma voxels from taking the brain tissue class[2]. 0.05 is a constant probability for other voxels, with the assumption that vessels occupy less then 5% of all brain voxels [3], [7]. $\mathcal{A}^{BG}$ is a basal ganglia atlas to penalize the vessel class inside hypointense basal ganglia nuclei such as the lenticular nuclei, substantia nigra, etc. Otherwise, these iron-rich nuclei may be incorrectly classified as vessels by the appearance and (to some extent) the shape potentials. See Appendix for additional details on the creation of the probabilistic atlases.

B. Interaction Potential

The interaction potential models contextual dependencies between all pairs of neighboring voxels. The interaction term is composed of a smoothness potential (V_{smooth}) and a data-dependent edge potential (V_{edge}):

$$V_2(x_i, x_j|Y) = -V_{smooth}(x_i, x_j) - V_{edge}(x_i, x_j|Y). \tag{11}$$

V_{smooth} penalizes dissimilarities between two neighbor voxels. V_{edge} penalizes similarities when the observations support the presence of an edge.

[1]SWI is sensitive to changes in magnetic susceptibility (∇_χ) at the boundary between deoxygenated blood and other brain tissue; inside a sufficiently large vein such as the superior sagittal sinus, ∇_χ is lower.

[2]Non-parenchyma voxels are temporarily classified vessels and cropped during post-processing (see Section III-D).

1) Smoothness Potential: The smoothness potential is defined as a standard Ising potential:

$$V_{smooth}(x_i, x_j) = \beta_{ij}\delta(x_i \neq x_j) \tag{12}$$

δ is the Kronecker delta function and β_{ij} is a penalty for dissimilar classification $(x_i \neq x_j)$. In many applications, β_{ij} is chosen constant. However, such isotropic configuration applied to SWI can eliminate many thin veins with a radius $< \eta_i$ because a majority of voxels in η_i are (correctly) classified as T. Instead, we implemented an anisotropic Ising potential with two possible values for β_{ij} (β_V and β_T), such that:

$$\beta_{ij} = \begin{cases} \beta_V & x_j = V; \beta_V \mathcal{N}_V(\eta_i) < \beta_T \mathcal{N}(\eta_i) \\ \beta_T & \text{otherwise} \end{cases}. \tag{13}$$

Note that $\beta_{ij} = \beta_V$ when $x_j = V$ and $\beta_{ij} = \beta_T$ when $x_j = T$. When $\beta_V > \beta_T$, it takes fewer voxels $x_j = V$ to change the classification of a voxel $x_i = T$ than in the isotropic case. Likewise, it takes more voxels $x_j = T$ to change the classification of a voxel $x_i = V$ than in the isotropic case. The condition $\beta_V \mathcal{N}_V(\eta_i) < \beta_T \mathcal{N}(\eta_i)$, where $\mathcal{N}_V(\eta_i)$ is the number of voxels classified as V in η_i and $\mathcal{N}(\eta_i)$ is the total number of voxels in η_i, cancels the anisotropic behavior to prevent over-segmentation when there is already enough voxels $x_j = V$ in η_i.

2) Edge Potential: The edge potential is modeled as follows:

$$V_{edge}(x_i, x_j|Y) = \alpha(1 - r_i^{leak}) f_{x_i \to x_j}(\nabla y_j \cdot \vec{n}_{ij}) \tag{14}$$

α weights the importance of V_{edge}. $f_{x_i \to x_j}(\cdot)$ is a data-dependent penalty term for similar classification $V \to V$ or $T \to T$ in presence of a signed edge (∇y_j) in the data:

$$f_{T\to T}(\nabla y_j \cdot \vec{n}_{ij}) = \begin{cases} 1 - \exp(-k\|\nabla y_j \cdot \vec{n}_{ij}\|) & (\nabla y_j \cdot \vec{n}_{ij}) > 0 \\ 0 & \text{otherwise} \end{cases}$$
$$f_{V\to V}(\nabla y_j \cdot \vec{n}_{ij}) = \begin{cases} 1 - \exp(-k\|\nabla y_j \cdot \vec{n}_{ij}\|) & (\nabla y_j \cdot \vec{n}_{ij}) < 0 \\ 0 & \text{otherwise} \end{cases} \tag{15}$$

∇y_j is the first-order image gradient at voxel $j \in \eta_i$. $\vec{n}_{ij}$ is a unit vector oriented along the edge formed by voxels i and j. Thus, $f_{x_i \to x_j}$ penalizes the pattern $(x_i, x_j) = (T, T)$, in the presence of a positive edge perpendicular to $\vec{n}_{ij}$. Similarly, $f_{x_i \to x_j}$ penalizes pattern $(x_i, x_j) = (V, V)$, in the presence of a negative edge perpendicular to $\vec{n}_{ij}$. k is a constant term that takes the value: $k = 0.5 \arg\max_i \|\nabla y_i\|$. This edge potential can detect fine, low-contrast, vessels with diameter $< \eta_i$ that could be missed by other potentials or smoothed out by V_{smooth}.

Fig. 3 illustrates the role of interaction potentials for improving strictly independent classification. A standard Ising-MRF potential (second column of Fig. 3) result in smoother segmentation, but it also misses fine veins. The combination of an Ising term and an edge term achieves both goals of regularizing the segmentation and detecting finer veins (green voxels in third column of Fig. 3). As illustrated in the second and third row of Fig. 3, most fine vessels branches detected by V_{edge} connect to a main branch making the segmentation robust to standard post-processing by connected-component analysis, commonly used in many cerebrovascular segmentation applications for removing small isolated clusters.

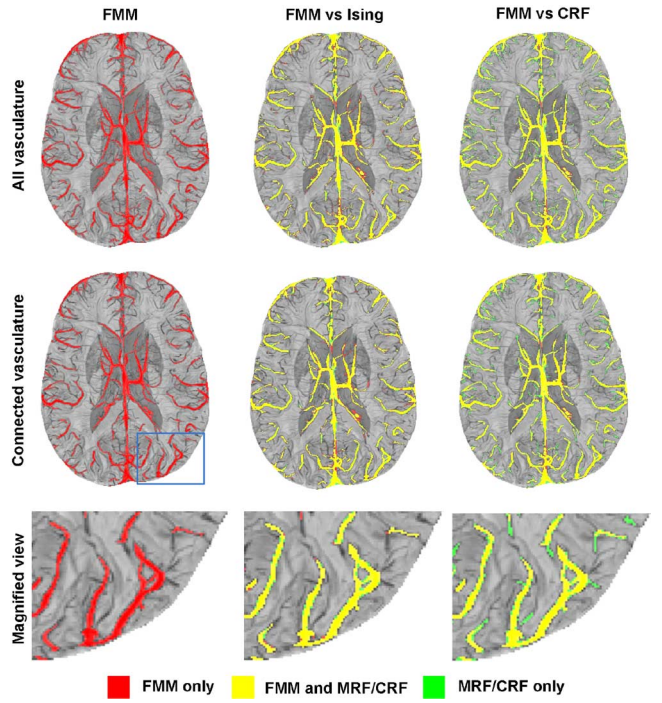

Fig. 3. Comparison of independent FMM, MRF-Ising and proposed CRF classifications. First column: independent FMM provides a coarse segmentation of the main vasculature (fine veins are only partially detected due to lower contrast). Second column: Standard MRF-Ising achieves smoother segmentation of the main vasculature but many fine veins are missed. Third column: The CRF achieves both smooth segmentation and detection of finer vasculature.

C. CRF Inference

Optimal classification X^* that maximizes $P(X|Y)$ is found by Iterated Conditional Modes (ICM) [31]. Hence, the CRF is solved iteratively by updating each classification x_i^k into x_i^{k+1} using:

$$x_i{}^{k+1} = \max_{l \in \{V,T\}} \left(V_1(x_i{}^k = l|Y) + \sum_{j \in \eta_i} V_2(x_i = l, x_j{}^k|Y) \right) \tag{16}$$

with

$$x_i{}^0 = \max_{l \in \{V,T\}} V_1(x_i = l|Y). \tag{17}$$

One limitation of ICM is that it cannot guarantee convergence to a globally optimal solution. However first-order potentials (V_1) provide an initial classification sufficiently close to converge to a desired ICM solution. Furthermore, the local ICM method can conveniently solve complex CRF models that may be difficult to solve using a global method, such as Graph Cuts, either due to the use of multi-neighborhood patterns [9], as in (13), or non-submodular energy, as in (15).

D. Post-Processing

The only post-processing needed is to exclude non-parenchyma tissue [28]. To do so, we estimate a convex parenchyma mask that preserves surface vasculature. This

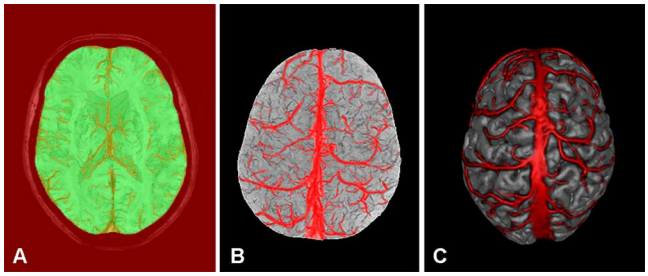

Fig. 4. Post-processing for skull-stripping and surface vessel visualization. (a) The computed parenchyma mask, in green, overlaid on the CRF segmentation, in red, to distinguish between vessels and non-brain voxels. (b)–(c) Visualization of surface veins by \min /max intensity projection by 3D volume rendering.

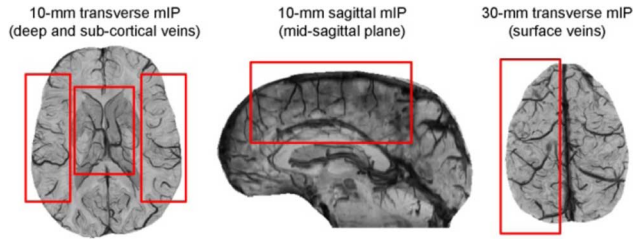

Fig. 5. Examples of regions-of-interests used to evaluate the performance of CRF segmentation: (left) deep and sub-cortical veins (center) veins near the mid-sagittal plane, (right) superficial veins.

mask is computed via a binary majority filter applied iteratively to the T class. Then, vessel concavities at the surface are detected using a modified ball filter [36] that measures the local widening within a large neighborhood R_i for all surface voxels x_i classified as V.

$$E_R(i) = E'_R(i) + x_i \sum_{j \in R_i} E'_R(j) \tag{18}$$

with

$$E'_R(\mathrm{i}) = \sum_{j \in R_i} X(x_j) \quad X(x_j) = \begin{cases} 0 & x_j = T \\ 1 & x_j = V \end{cases}. \tag{19}$$

Vessel concavities are detected by computing the ball measure twice, once with $R_i = sphere$ (a standard sphere shape centered at x_i) and once with $R_i = sheet$ (a local 3D sheet-like shape of the brain surface also centered at x_i), to verify that $E_{R=ball}(i) \gg E_{R=sheet}(i)$ to exclude remaining flat patches at the surface that were not eliminated by the binary parenchyma mask. Fig. 4 illustrates the post processing step. Fig. 4(a) shows a computed parenchyma mask over the inferred CRF segmentation. Fig. 4(b) shows the surface veins as maximum intensity projection (MIP) over on a minimum intensity projection (mIP) of the raw data. This view qualitatively confirms that the segmentation matches the vasculature exhibited by the raw data. Fig. 4(c) shows a 3D rendering view of the surface vasculature for integration with the surgical workflow.

IV. Experiment

A. MRI Acquisition and Preprocessing

SWI datasets were acquired on a 3T Siemens TIM Trio scanner with a 32-channel head coil on a total of 30 DBS patients (14 males, 16 females, age range $= [43\text{-}73]$, mean $= 58$, SD $= 8.4$). We used a multi-echo acquisition strategy to increase signal-to-noise ratio as described by Denk *et al.* [37]. Thus, SWI magnitude and phase datasets were obtained from a 3D gradient echo sequence with axial orientation, $0.5 \times 0.5 \times 1$-mm resolution, 5 equally spaced echo times (TE) within the range 13-41 ms, a repetition time (TR) of 48 ms and a flip angle (α) of 17° for a total acquisition time of 10:24 minutes using GRAPPA acceleration (factor of 2). The first echo is fully flow compensated. The third and fifth echoes are flow compensated in the readout direction. Magnitude and phase images from each echo are combined by standard SWI reconstruction [2] and averaged. T1w anatomical contrast of the whole head was also acquired using a 3D, magnetization-prepared, rapid gradient-echo (MP-RAGE) sequence with sagittal orientation and $1 \times 1 \times 1$-mm resolution (TR $= 2300$ ms, TE $= 2.98$ ms, TI $= 900$ ms, $\alpha = 9°$, iPAT $= 2$, acquisition time $= 5:30$ min). T1w and SWI datasets, both acquired during the same scanning session, were rigidly registered by mutual information.

T1w datasets were corrected for intensity non-uniformity using N3 [38], normalized across all subjects by histogram matching [39] and processed with BEaST [40] to extract a brain mask ($\mathcal{M}$). The SWI datasets were resampled to 0.5-mm isotropic resolution, denoised with a non local means algorithm [41], [42] and corrected using N3 [38]. SWI intensities were linearly scaled to match intensity histogram peak across all subjects. Both T1w and SWI contrasts are used to deform the probabilistic atlases $\mathcal{A}^{BG}$, $\mathcal{A}^{sinuses}$, $\mathcal{A}^{skin}$ to the patient's anatomy (see Appendix).

All SWI datasets were manually segmented by one expert rater. A subset of 5 datasets was re-segmented by the same rater and by a second rater to estimate the intra- and inter-rater variability. The segmented datasets were randomized and separated in two pools: training and testing pools. The training pool contains 15 datasets, which are used for atlas creation and CRF parameter estimation (see Section IV-B). The testing pool contains the other 15 datasets, which are used to evaluate the CRF segmentation's performance (see Section IV-C).

Manual segmentation of whole-brain 3D SWI data can be considered intractable. Nowinski *et al.* [43] reported that manually segmenting much sparser TOF MRA datasets can necessitate as much as 8 weeks of manual labor per subject. Our solution was to segment 2D minimum intensity projection (mIP) slabs that focus on specific vascular system of interest: deep venous system (10-mm transverse slab—Fig. 5(a), left and right sub-cortical veins (two 10-mm transverse slabs—Fig. 5(a), veins near the inter-hemispheric fissure (10-mm sagittal slab—Fig. 5(b) and surface veins (30-mm transverse slab—Fig. 5(c) for a total of 150 segmentation examples (5 per subjects). To compare 3D automatic segmentation against 2D manual segmentation, we compute 2D maximum intensity projection (MIP) of the 3D segmented data. Quantitative comparison metrics that we used are:

TABLE I
SUMMARY OF ALL USER PARAMETERS ESTIMATED DURING THE CRF TRAINING PHASE

User variable	Recommended value	Reason
Appearance Potential		
(none)	(none)	There are no user parameters for the appearance potential.
Shape Potential		
Vesselness (α,β,γ)	$\alpha = 0.5, \beta = 0.5, \gamma = 0.5 \underset{i}{\operatorname{argmax}}\|\mathcal{H}_i\|$	Default parameters as described in Frangi et al.'s. These parameters work well in practice.
Vesselness scales (σ, $\nabla\sigma$)	$\sigma = [0.5 - 2.5]$, $\nabla\sigma = 0.25$	Small scales are used for the vesselness. This enables detection of fine vasculature in SWI.
Objectness scales (σ, $\nabla\sigma$)	$\sigma = [2.0 - 8.0]$, $\nabla\sigma = 1.0$	Larger scales are used for the generalized objectness. This tunes the objectness for the detection of large plate-like regions of signal loss (anti-pattern).
Shape potential's b	$b = 0.08$	Moves the sigmoid to an appropriate decision boundary for the vesselness. Hence, $\sigma(\mathcal{V}_i) > 0.5$ when $b > 0.08$.
Shape potential's a	$a = 70$	Modulates the global fuzziness of the sigmoid. Increasing a will give more weight to the shape potential (ψ) over other potentials.
Location Potential		
ANIMAL's registration parameters	See TABLE III	Different atlas registration steps (step size/blurring kernel in particular) can be used for controlling the overall fuzziness (and importance) of location prior.
Interaction Potentials		
Smoothness potential's β_T and β_V	$\beta_T = 0.8, \beta_V = 2.4$	Weights the importance of V_{smooth} interaction. Increasing β parameters will result in a smoother segmentation, but could also erase smaller veins. $\beta_V > \beta_T$ is used to prevent oversmoothing smaller veins.
Edge potential's α	$\alpha = 6$	Weights the importance of V_{edge} interaction. Increasing this parameter enables detection of small low-contrast veins, but could also introduce noise due to inclusion of non-vessel edges.

— The Dice-kappa coefficient [44], which measures the agreement between automatic and manual segmentation. Specifically, it measures how well the automatic segmentation matches the manual segmentation on a voxel-by-voxel (i.e., hit-or-miss) basis. Consequently, larger vessels will necessarily have a stronger influence. This limitation is mitigated by computing the kappa coefficients regionally on smaller ROIs.

— The alignment error, which measures the Euclidean distance between each vessel voxel in the manual segmentation and the closest vessel voxel in the automatic segmentation and vice-versa. This metric was previously used in [45] but only the average alignment error was reported and in a single direction (manual to automatic segmentation). This metric explains the disagreement between the automatic and manual segmentations. Specifically, it quantifies spatial differences related to the estimation of the vessel-tissue boundary in the two segmentations. It is also sensitive to differences in segmentation of thin vessels because of the higher surface-to-volume ratio.

B. CRF Parameter Estimation

The CRF model described in Section III comes with a number of parameters that must be estimated. Optimal parameters are summarized in Table I. They were determined using the segmentation examples of the training pool via a piecewise learning approach [46] (see Appendix for the details).

C. Validation

The performance of the trained CRF model was then validated using the other 15 SWI datasets in the testing pool. As such, kappa similarity and alignment error metrics were computed on all 75 segmentation examples in the testing pool. For comparison, these validation metrics were also computed on alternate segmentations obtained from different intensity and shape potentials taken individually. Specifically, we validated against: 1) Frangi *et al.*'s vesselness[3] [14], 2) multi-scale spherical flux (S-Flux)[4] [16], [17], and 3) optimally-oriented flux (O-Flux)[5] [18]. The vesselness potential was computed as per Table I. S-Flux and O-Flux potentials were computed over 10 radii ($\min = 0.5$ mm, $\max = 2.5$ mm). These alternate segmentations were thresholded to maximize the kappa overlap with the ground truth. In other words, we compared our CRF (computed without knowledge of the manual segmentation) with the maximal overlap that can be achieved by any of these alternate potentials if the manual segmentation is known. CRF segmentation is also compared to standard MRF segmentation to evaluate the effect of the data-dependent interaction term (V_{edge}).

V. RESULTS

A. Quantitative Validation

The box-plots of Fig. 6 shows kappa coefficients between different automatic segmentations and the manual segmentation, across all 15 test subjects, for deep venous systems (15 test samples), left and right sub-cortical veins (30 test samples), mid-sagittal plane (15 test samples) and surface vasculature (15

[3]Implementation available online at: http://www.mathworks.com/matlabcentral/fileexchange/24409-hessian-based-frangi-vesselness-filter

[4]Implementation available online at: http://www.mathworks.com/matlabcentral/fileexchange/41108-efficient-implementation-for-spherical-flux-computation--3d-

[5]Implementation available online at: http://www.insight-journal.org/browse/publication/885

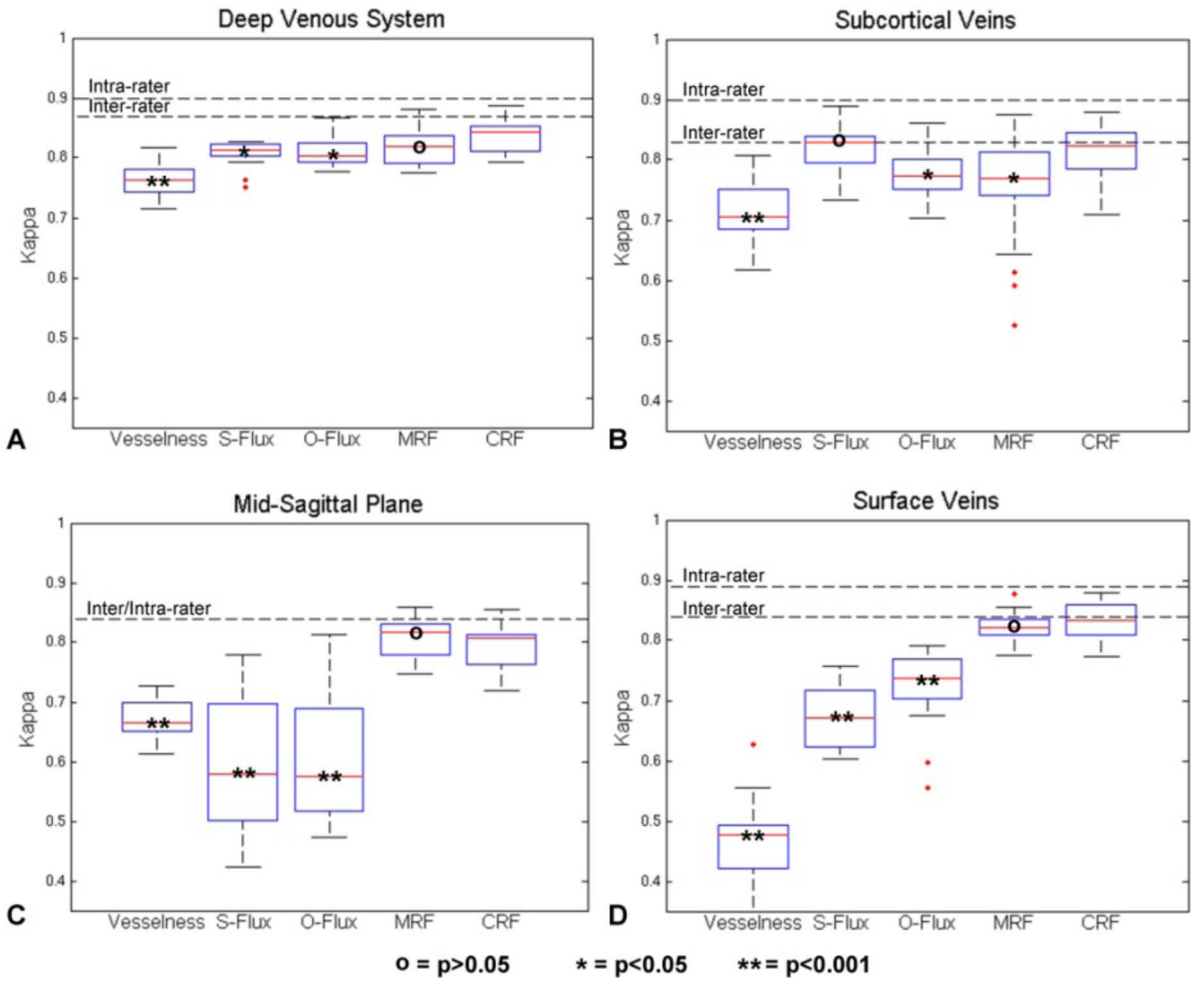

Fig. 6. Kappa coefficients between manual and different automatic SWI segmentation (vesselness, S-Flux, O-Flux, MRF, CRF) for different brain areas: (a) deep venous system (b) sub-cortical veins, (c) mid-sagittal plane (d) surface veins.

TABLE II
MEDIAN INTER-RATER AND INTRA-RATER VARIABILITY FOR DIFFERENT REGIONS-OF-INTEREST

Region-of-interest	Intra-rater	Inter-rater
Deep venous system	0.90	0.87
Sub-cortical veins	0.90	0.83
Mid-sagittal plane	0.84	0.84
Surface veins	0.89	0.84

test samples). Median intra-rater and inter-rater variability results are shown in Table II. The high values indicate that the manual segmentations can be used to validate the proposed automatic technique.

Fig. 7 compares the alignment error between the different automatic segmentations and the manual segmentation symmetrically. The left column illustrates the computed alignment error as a histogram. The "0 mm" bin describes the % of vessel voxels with exact alignment. The "$<$ 1 mm", "1-2 mm" and "$>$ 2 mm" bins describe the % of voxels misaligned by, respectively, less then 1-mm, less than 2-mm and more than 2-mm. In other words, the "0 mm" bin contains voxels classified as vessels in the automatic and manual segmentation datasets (i.e., true positives). The "$<$ 1 mm" and "1-2 mm" bins contain false-positives and false-negatives voxels at a small distance of a true-positive (i.e., errors near the vessel boundary). The "$>$ 2 mm" bin contains voxels at a large distance from a true positive. This last bin describes errors such as missing a branch or segmentation of non-vessel tissue (e.g., leaks, noise, etc.). The right column of Fig. 7 computes the Earth Mover's Distance (EMD) [47] between the CRF histogram and other segmentations' histograms. A positive EMD means that the CRF histogram is shifted towards left (low-error) bins in comparison to the alternate segmentation. Thus, a positive EMD indicates that the CRF segmentation has a smaller alignment error.

Non-parametric two-tailed Wilcoxon tests are used for all comparisons in Figs. 6 and 7. In comparison to vesselness segmentation, the CRF significantly improves ($p < 0.001$) the kappa overlap and alignment error in all regions-of-interests. In comparison to flux-based segmentation, the CRF yields comparable or improved ($p < 0.05$) segmentation within deep and sub-cortical areas, and significantly improves ($p < 0.001$) the kappa overlap and alignment error at the midline and brain surface.

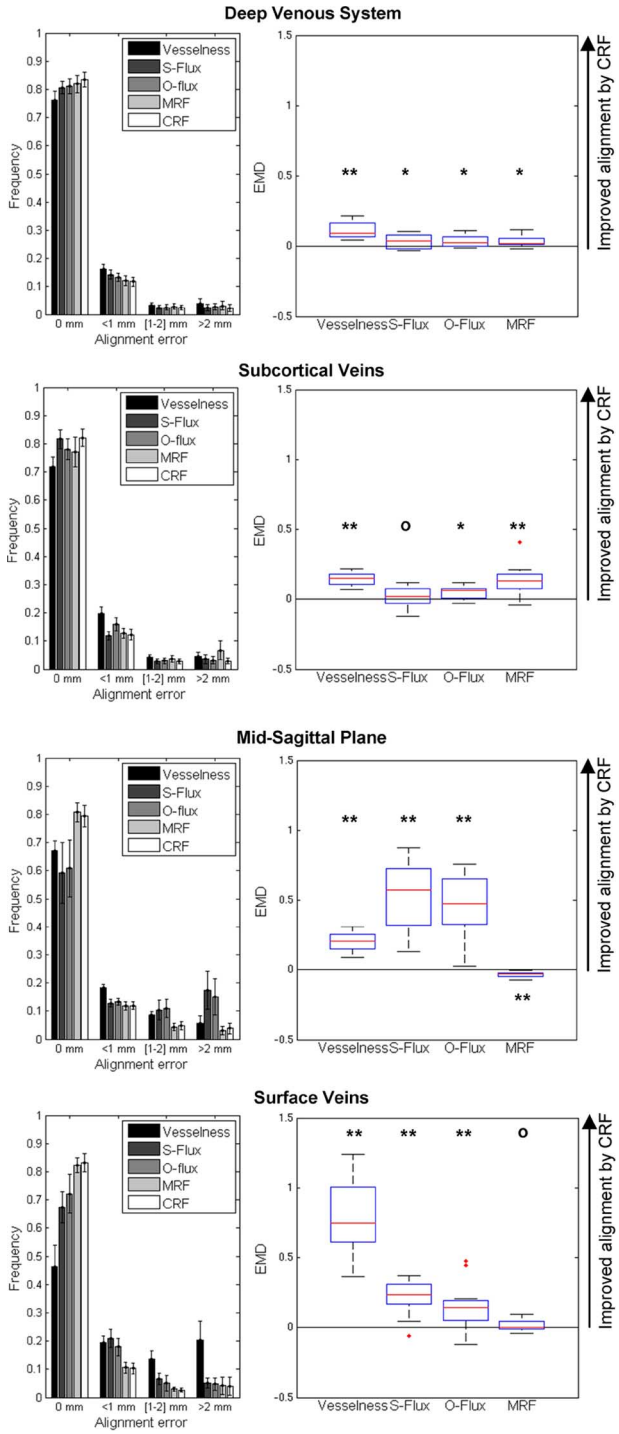

Fig. 7. Alignment errors between manual and different automatic segmentation (Vesselness, S-Flux, O-Flux, MRF, CRF) for: (row 1) deep venous systems, (row 2) sub-cortical veins, (row 3) mid-sagittal plane and (row 4) surface veins. The left column shows histograms of alignment errors computed over all test subjects. The right column shows comparison between CRF and Vesselness/S-Flux/O-Flux/MRF histograms using the earth mover's distance (EMD). Positive EMD indicates that the CRF histogram is shifted to the left relatively to the alternate segmentation. $(^*)p < 0.05$, $(^{**})p < 0.001$, $(o)p > 0.05$.

The difference between data-dependent CRF and standard MRF is subtle because it relates to the detection of fine vessels that have little effect on the overall kappa except in sub-cortical regions that are dominated by smaller vessels. Differences between CRF and MRF are best detected by comparing the alignment errors. As such, CRF segmentation improves the alignment error in general-purpose deep venous system $(p = 0.001)$ and sub-cortical $(p < 0.001)$ regions. On the counter part, higher alignment error is observed at the midline $(p < 0.001)$.

Fig. 8 shows median CRF segmentation results for each ROI. In deep and sub-cortical ROIs, only few low-contrast 1-voxel thick vessels (0.5 mm diameter) are missed or partially detected. The simpler MRF model tends to miss more vessels as indicated (black circles). CRF and MRF segmentations in the mid-sagittal plane are qualitatively similar and tend to detect more vessel branches than identified in the manual segmentation. These finer vessels are not necessarily false-positives as they could have been partially hidden by the hypointense inter-hemispheric fissure during the mIP operation and thus difficult to segment manually. CRF is particularly effective at segmenting these fine hidden vessels, which could also explain the increase in alignment error illustrated in Fig. 7. Finally, all major surface veins are correctly segmented by CRF and MRF. Few smaller branches are missed, in part due to skull stripping.

B. Qualitative Validation

Fig. 9 illustrates CRF segmentation of a single subject in comparison to alternate segmentation based on vesselness, S-Flux and O-Flux potentials.

The first row of Fig. 9 shows segmentation of a standard 20-mm transverse SWI slab exhibiting deep venous and sub-cortical venous systems. Comparable segmentation is obtained for CRF and flux-based segmentation. In the sub-cortical area especially, the background tissue is relatively uniform and highly contrasting thus allowing gradient-based S-Flux and O-Flux to detect very fine vasculature. CRF also segments fine vessels because of the data-dependent gradient interaction term. Classification based strictly on Hessian-based vesselness filtering is less sensitive to finer vessels and it is difficult to precisely segment the vessel-tissue boundary. This is because the vesselness response is strong near the centerline, where the tubular model is best matched, and ambiguous (threshold-dependent) at vessel boundary. This observation is consistent with lower kappa overlap and higher alignment errors observed for vesselness-based segmentation.

The second row of Fig. 9 shows segmentation of a 10-mm sagittal slab taken medially to exhibit signal loss due to the interhemispheric space. Clearly, flux-based methods are not suitable in that region. This explains the low kappa agreement and high alignment errors obtained for S-Flux and O-Flux. Hence, segmentation near the mid-sagittal plane necessitates a stronger tubular shape model. Hessian-based vesselness filtering effectively segments veins hidden by other sources of signal loss at the midline but undersegments large vessels such as the superior sagittal sinus and straight sinus also present in this slab. CRF segmentation that combines a Hessian-based shape potential and an atlas location potential can detect both large veins and smaller veins partially obscured by interhemispheric signal loss.

The third row of Fig. 9 shows segmentation of a 30-mm slab taken at the brain surface near the apex. These superficial veins do not exhibit full 3D tubular contrast because the skull is hypointense. For this reason it is particularly challenging to apply

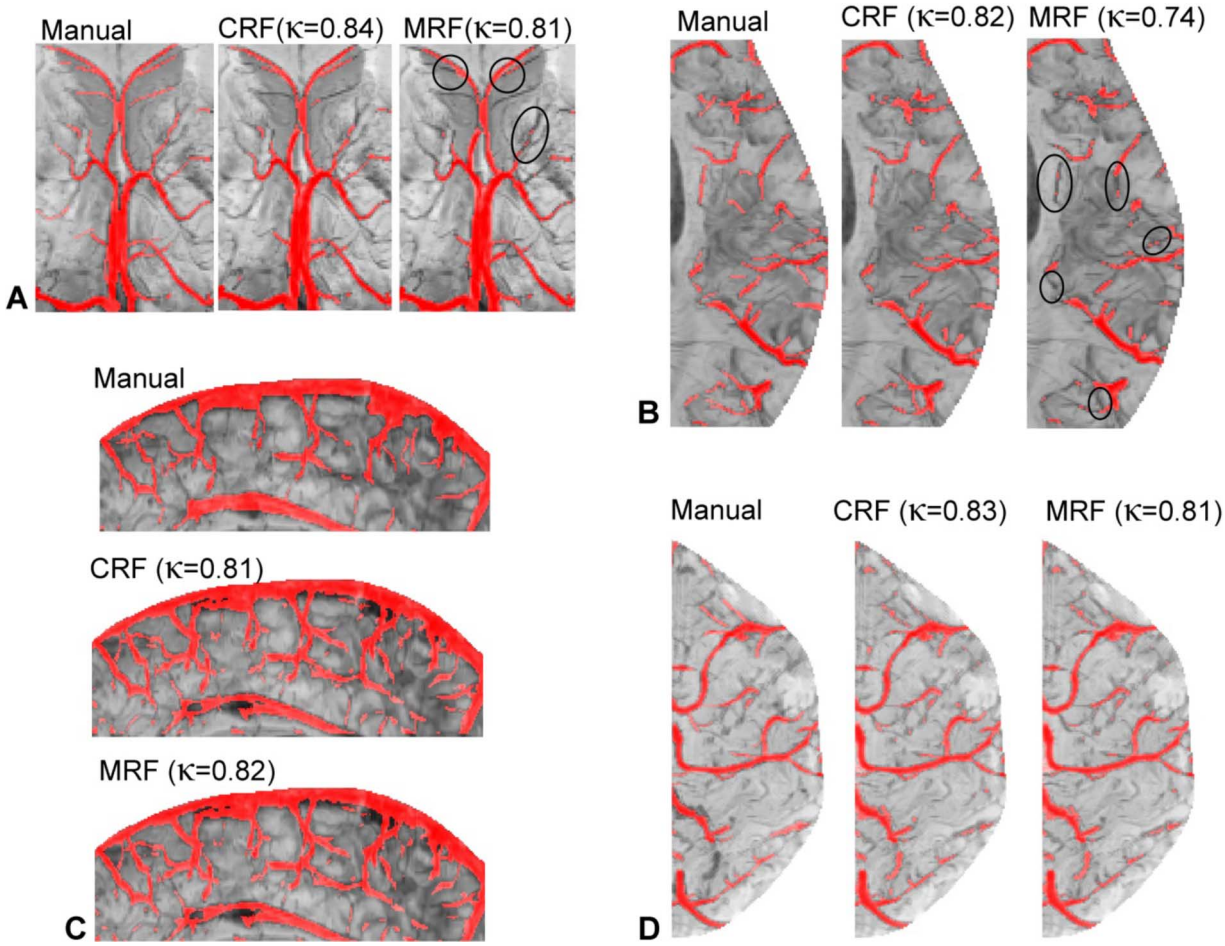

Fig. 8. Manual, CRF and MRF segmentations in each region-of-interest: (a) deep venous system, (b) sub-cortical veins, (c) mid-sagittal plane, (d) surface veins. For each ROI, the segmentation with median CRF-kappa overlap is shown. The circles indicate specific vessel branches in deep and sub-cortical ROIs that were mis-segmented in MRF (i.e., missed or partially detected vessels) and improved by CRF segmentation.

a shape potential without undersegmenting the superficial veins. This explains the lower kappa overlap and higher alignment errors observed for all other potentials. Since Hessian-based filtering imposes stricter shape constraints in comparison to gradient-based S-Flux and O-Flux, it is the least suitable potential for superficial vein segmentation.

Additional examples on different subjects are shown in Fig. 10 to demonstrate the generality of the proposed solution. Note that the raw SWI datasets (first row of Fig. 10) were acquired on a population of elderly Parkinson's patient and the raw image quality varies due to possible patient motion (e.g., tremors). Subject 1 is the most degraded dataset. Subject 3 is the highest quality and most dense dataset. CRF segmentation provides robust and consistent segmentation on all these cases.

In these examples, it is important to note that SWI acquisitions are inherently qualitative as they tend to exaggerate vessel size. This can be seen in the raw data (e.g., first column of Fig. 9, first row of Fig. 10) and, consequently, in the CRF segmentation (last column of Fig. 9, second row of Fig. 10). Indeed, SWI exploits phase changes occurring at the boundary between tissues with different magnetic susceptibility. By enhancing the interface between veins and tissue, SWI exaggerates vessel size, but also enables visualization of finer veins that are otherwise invisible in conventional MRA.

VI. Discussion and Conclusion

Minimizing the risk of damaging the cerebral vasculature is essential in many neurosurgical procedures. Advanced MR venography techniques such as SWI can provide definitive advantages over traditional gadolinium-based MRI for imaging finer venous structures [3]. However, current clinical segmentation protocols are impractical for dense SWI venograms, especially when large brain coverage is needed. This study demonstrates that a CRF model with an energy function that aggregates different 1^{st} and 2^{nd} order potentials (appearance, shape, location, Ising interaction, and data-dependent interaction) is suitable for automatic, robust, whole-brain SWI segmentation. Our results show that the aggregated CRF approach effectively segments veins within deep venous and sub-cortical areas, and improves segmentation of more challenging brain regions near the midline and at the brain surface.

The 3D CRF model was trained and validated using 2D min/max intensity projection (MIP) space due to feasibility constraints for generating reliable manual segmentation of very dense SWI vasculature with acceptable (low) intra- and inter-rater variability. This comes without any loss of generality and we tested the segmentation using multiple MIP orientations: transverse and sagittal. The segmentation examples used for training and testing the CRF segmentation were

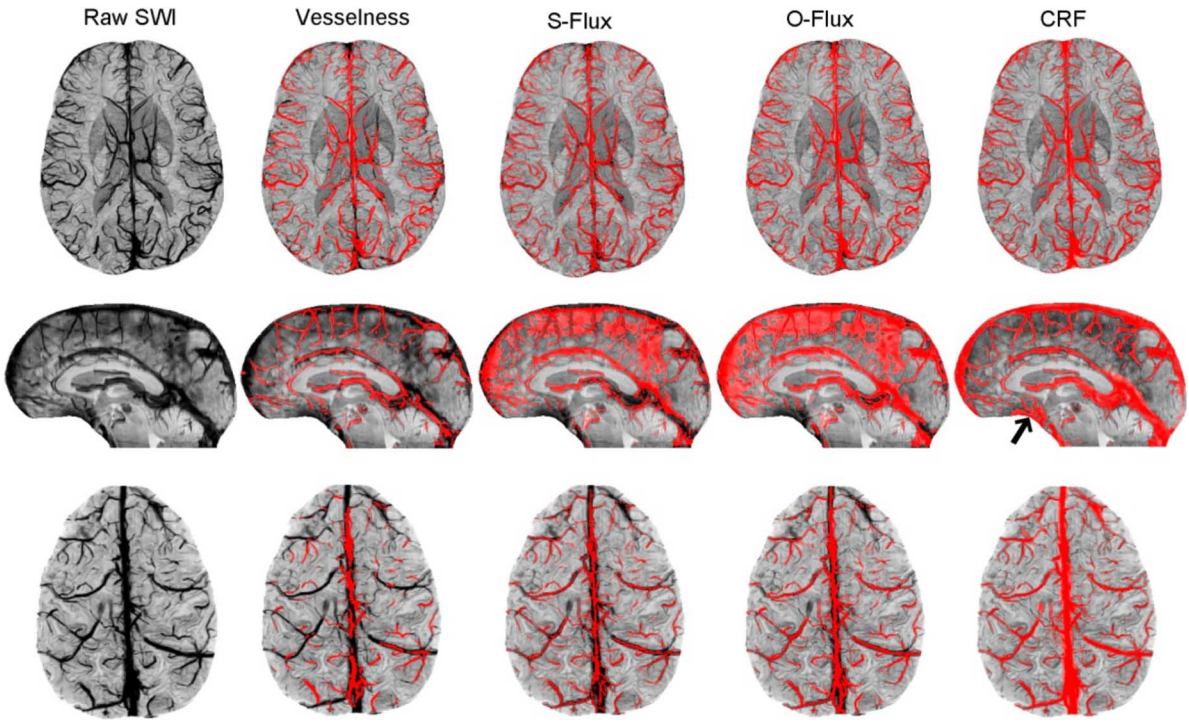

Fig. 9. Comparison of binary SWI segmentation using Frangi et al's vesselness, spherical flux (S-Flux), optimally oriented flux (O-Flux) and the proposed CRF. (row 1) standard 20-mm transverse MIP taken at the level of the lateral ventricles. (row 2) 10-mm sagittal MIP at the inter-hemispheric fissure. (row 3) 30-mm transverse MIP at the brain surface.

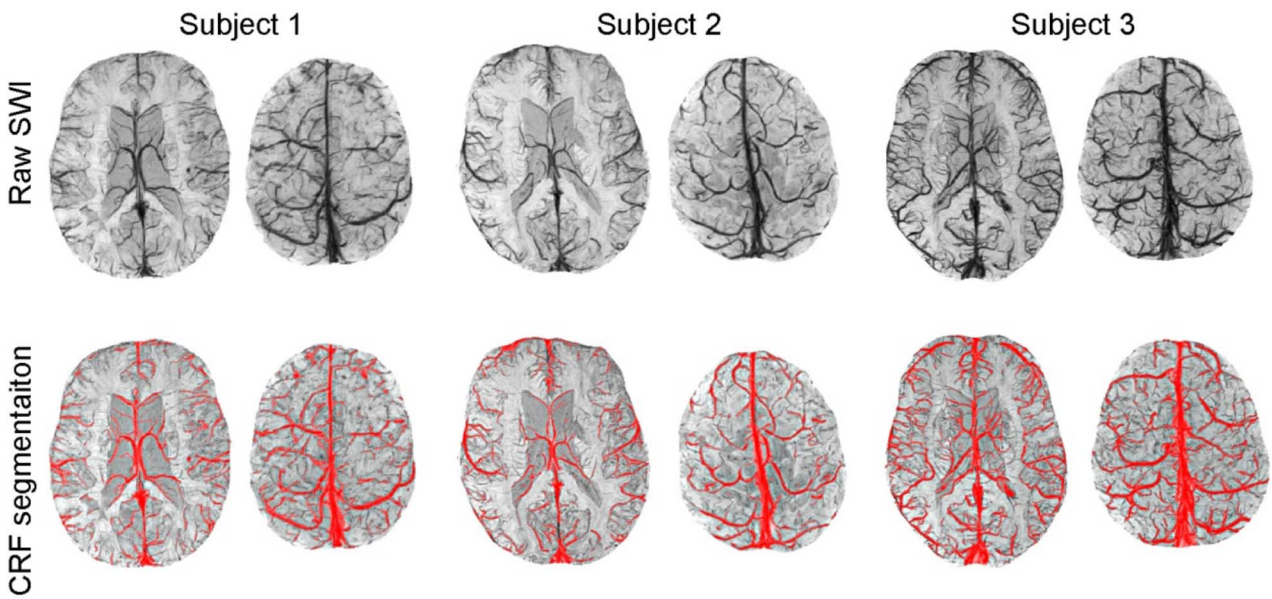

Fig. 10. Additional CRF segmentation examples exhibiting consistent results across different subjects. Note that subject 1's dataset is degraded due to patient motion.

all manually delineated using ITK-SNAP [48], without any pre-segmentation that could bias the manual segmentation.

Quantitative validation metrics used in this work include standard Dice-kappa overlap and alignment errors. The kappa metric measures the agreement between manual and automatic segmentation, but does not measure how far "disagreeing" voxels (i.e., false-positives and false-negatives) are from the closest "agreeing" vessel voxels. This is measured by the alignment error analysis. Other related works previously reported the mean alignment error [45], which only provides partial information about the alignment error, or the maximal alignment error [11], which can be too sensitive to isolated false-positives that are trivial to exclude by post-processing. In this work, the alignment error was presented as a complete histogram. This revealed that the aggregated CRF segmentation comes with fewer "disagreeing" voxels and the disagreement is also smaller in distance in comparison to segmentation based on a single potential. Illustrative segmentation examples

further demonstrate the generality of the segmentation across the different brain regions.

One limitation of the current CRF model is the sensitivity to susceptibility artifacts observed near air-tissue interfaces (e.g., nasal cavities and ear canal) and specifically near the orbito-frontal cortex (black arrow in Fig. 9, second row) and within inferior temporal lobes (not shown). This is a limitation of the SWI method itself and additional location potentials could be incorporated for excluding these artifacts from the final segmentation. It is important to note that alternate angiography modalities should be considered for applications that necessitate exploration or inferior temporal lobes or orbito-frontal cortex [3].

Another limitation of our SWI acquisition strategy is that the second and fourth echoes are not flow compensated. As noted by Denk *et al.* [37] large arterial vessels may experience signal loss due to fast flow in these non-flow compensated echoes and could be mistaken for veins by our CRF. However, 3 out of 5 echoes being averaged are flow compensated, and we found this sufficient to provide robust preservation of signal from the arteries, at least for brain regions dorsal to the circle-of-Willis. In larger arteries below this level it is also important to note that SWI is not the most convenient modality because of air-tissue interface susceptibility artifacts. A potential future work could consist of adding arterial-dominated TOF contrast as input to the CRF model for superior separation between veins and large arteries in ventral brain regions.

By design, this CRF model applies to reverse-contrast SWI acquisitions. Specifically this CRF was trained and evaluated using a multi-echo SWI acquisition protocol. However, the same CRF model also applies to more conventional single-echo SWI acquisitions, either by re-training the CRF or using the default parameters summarized in Table I. The advantage of a multi-echo acquisition strategy is the higher signal-to-noise ratio obtained due to the averaging of signal from the multiple echo times, which enhance visualization and detection of very fine sub-cortical veins. The main disadvantage of the multi-echo acquisitions is that longer TEs accentuate T2*-weighted contrast and signal attenuation in basal ganglia structures with higher iron content. This limitation is mitigated by the use of location priors that penalize the vessel class inside iron rich basal ganglia nuclei.

Furthermore, this CRF model was designed to segment datasets that follow a standard SWI reconstruction process. As such, the information obtained from the phase and magnitude of the MRI is merged together, by applying an independent voxel-wise operation to voxels with negative phase, to produce a new susceptibility-weighted contrast. This comes with the advantage that our CRF model applies to off-the-shelf SWI acquisitions as implemented by most MRI manufacturers. However, our raw data consisted of 5 echoes with separate magnitude and phase data that provide extra, potentially valuable, information for vessel segmentation. A number of variants of our CRF could therefore be explored as future work. One variant could consist of treating the intensities specific to each echo as a vector of observations rather than a signal average, since each echo time produces different T2*-weighted contrast. Another variant could consist of processing the magnitude and phase of the MRI echoes separately. In particular, additional CRF potentials could be designed to detect advanced phase patterns, spatially and across different echo times, that may better describe the venous vasculature.

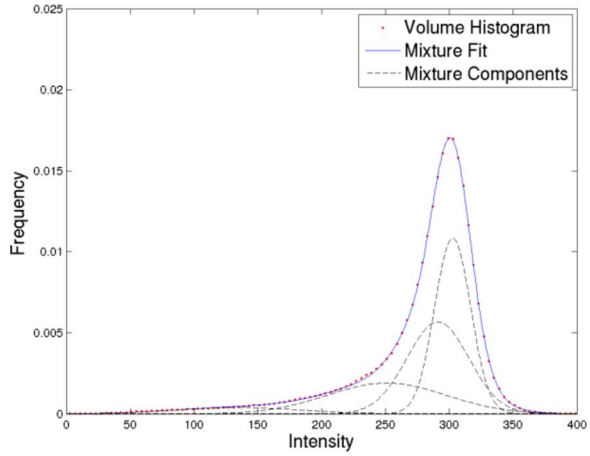

Fig. 11. Typical brain intensity histogram on SWI data (red dots) and EM fitting (blue line) of a Finite Mixture of 4 normal distributions (dashed lines).

In summary, this paper described an automatic CRF segmentation for SWI venography datasets and that improves classification based on a single potential. Patient-specific 3D modeling of the cerebral veins finds potential application in minimally invasive interventions for planning safe key-hole trajectories and other non-surgical applications, for example, in fMRI studies to screen for significant venous structures that might be within areas of blood oxygenation level-dependent (BOLD) activations [26].

APPENDIX
PIECE-WISE CRF TRAINING

Piece-Wise Training for the Appearance Potential: There are no free parameters to estimate for the Appearance Potential. However, the EM requires some initialization. Since SWI intensities are normalized across all subjects, fixed parameters were used to initialize the 3 normal distributions that model the tissue intensities. Initial parameters for the vessel class are determined by simple thresholding of vesselness filtered SWI ($\mathcal{V}$). As illustrated in Fig. 11, the FMM is accurately fitted to the intensity histogram with an absolute error of 0.0230 ($\mathrm{SD} = 0.0134$) that compares well with values previously reported in other MRA applications [7].

Piece-Wise Training for the Shape Potential: Internal vesselness parameters were initialized as suggested in [14] ($\alpha = 0.5$, $\beta = 0.5$, $\gamma = 0.5 \arg\max_i \|\mathcal{H}_i\|$). The vesselness measure was computed over multiple scales within the range $\sigma = [0.5 - 2.5](\nabla\sigma = 0.25)$. These parameters work well in practice. Similar internal parameters were used for the objectness measure ($\mathcal{O}$) of (8), but with higher scales $\sigma = [2.0 - 8.0](\nabla\sigma = 1.0)$ to detect large non-vessel patches of signal loss.

The shape potential, as described in (7)–(9), requires estimation of two parameters (a and b).

— Parameter b is learned by thresholding $\mathcal{V}$ to maximize the kappa coefficient over all training examples. Thus, we used $b = 0.08$.

TABLE III
MULTI-CONTRAST NON-LINEAR REGISTRATION PARAMETERS. ITERATIONS 1–20 USE T1W CONTRAST AND ACHIEVE COARSE-TO-FINE BRAIN ALIGNMENT. ITERATIONS 21–24 USE SWI CONTRAST AND ACHIEVE FINE VASCULAR ALIGNMENT

Iteration	Step size (mm)	Blurring kernel (mm)	Neighborhood size (mm)	Contrast
1-4	32	16	96	T1w
5-8	16	8	48	T1w
9-12	8	4	24	T1w
13-16	4	2	12	T1w
17-20	2	1	6	T1w
21-24	2	1	6	SWI

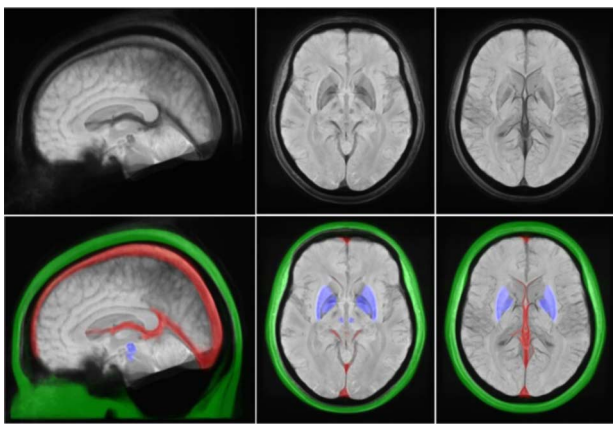

Fig. 12. Location potential defined on a non-linear 15-subjects SWI atlas. (first row) Different slabs of the raw multi-subject atlas. (second row) The probabilistic atlases: red scale = $\mathcal{A}^{sinuses}$, blue scale = $\mathcal{A}^{BG}$, green scale = $\mathcal{A}^{skin}$.

— Parameter a is learned by classifying all training dataset using the first-order (association) potentials while increasing a within the range [0-100] with a step size of 5. a is chosen to maximize the kappa overlap at the inter-hemispheric fissure without scoring worse in deep venous system or sub-cortical areas. Thus, we used $a = 70$.

Piece-Wise Training for the Location Potential: We used an existing atlas for $\mathcal{A}^{skin}$ [49]. $\mathcal{A}^{sinuses}$ and $\mathcal{A}^{BG}$ were defined by creating a non-linear T1w-SWI template using the 15 subjects of the training pool as described next.

The T1w datasets were linearly transformed to stereotactic space using a 9-parameters affine transformation. Then, a non-linear T1w template was created using an iterative technique previously described and validated in [50]. Finally, a non-linear SWI template was created to further improve vasculature alignment. All registration iterations are achieved using ANIMAL [51] and Table III provides a brief summary of the registration parameters used at each step.

Large sinuses were manually segmented on the multi-subject SWI template, warped back into non-linear T1w-space separately for all 15 subjects and averaged to yield $\mathcal{A}^{sinuses}$. In other words, iterations 21–24 of Table III are inverted to cancel vasculature-related deformations, thus modeling inter-subject vascular variability, while keeping other brain deformations. $\mathcal{A}^{BG}$ is processed similarly, except that we inverted all non-linear deformations (iterations 1–24). Fig. 12 illustrates the 15-subjects SWI average (first row) and the three location potentials (second row).

Piece-Wise Training for the Interaction Potential: The interaction potential parameters: α, β_V, β_T are estimated using the complete CRF.

— The ratio β_V/β_T of asymmetry is selected to balance the number of $V \rightarrow T$ and $T \rightarrow V$ label changes before and after ICM in sub-cortical regions that are characterized by the presence of many small veins.

— Similarly to [30], we varied the values of α in the range $[0, 10]$ and β_T in the range $[0, 1.8]$, and computed the average kappa and false-positive rate over all deep and sub-cortical training examples. Over all pairs (α, β_T), we selected α to maximize the kappa overlap and β_T to minimize the FP rate.

We used $\alpha = 6, \beta = 0.8$ and $\beta_V = 3.0\beta_T$. This β_V/β_T ratio is consistent with previous findings based on the pseudo-likelihood estimate [28].

REFERENCES

[1] E. M. Haacke *et al.*, "Susceptibility weighted imaging (SWI)," *Magn. Reson. Med.*, vol. 52, no. 3, pp. 612–8, Sep. 2004.

[2] E. M. Haacke *et al.*, "Susceptibility-weighted imaging: Technical aspects and clinical applications, Part 1," *AJNR Am. J. Neuroradiol.*, vol. 30, no. 1, pp. 19–30, Jan. 2009.

[3] S. Bériault *et al.*, "Neuronavigation using susceptibility-weighted venography: Application to deep brain stimulation and comparison with gadolinium contrast," *J. Neurosurg.*, vol. 121, no. 1, pp. 131–41, 2014.

[4] D. Lesage *et al.*, "A review of 3D vessel lumen segmentation techniques: Models, features and extraction schemes," *Med. Image Anal.*, vol. 13, no. 6, pp. 819–45, Dec. 2009.

[5] C. Kirbas and F. Quek, "A review of vessel extraction techniques and algorithms," *ACM Comput. Surv.*, vol. 36, no. 2, pp. 81–121, 2004.

[6] D. L. Wilson and J. A. Noble, "An adaptive segmentation algorithm for time-of-flight MRA data," *IEEE Trans. Med. Imag.*, vol. 18, no. 10, pp. 938–45, Oct. 1999.

[7] M. S. Hassouna *et al.*, "Cerebrovascular segmentation from TOF using stochastic models," *Med. Image Anal.*, vol. 10, no. 1, pp. 2–18, Feb. 2006.

[8] J. T. Hao, M. L. Li, and F. L. Tang, "Adaptive segmentation of cerebrovascular tree in time-of-flight magnetic resonance angiography," *Med. Biol. Eng. Comput.*, vol. 46, no. 1, pp. 75–83, Jan. 2008.

[9] S. Zhou *et al.*, "Segmentation of brain magnetic resonance angiography images based on MAP-MRF with multi-pattern neighborhood system and approximation of regularization coefficient," *Med. Image Anal.*, vol. 17, no. 8, pp. 1220–35, Dec. 2013.

[10] M. S. Hassouna *et al.*, "Statistical cerebrovascular segmentation for phase-contrast MRA data," in *Proc. Int. Conf. Biomed. Eng.*, 2002, pp. 101–105.

[11] M. Freiman *et al.*, "Carotid vasculature modeling from patient CT angiography studies for interventional procedures simulation," *Int. J. Comput. Assist. Radiol. Surg.*, vol. 7, no. 5, pp. 799–812, Sep. 2012.

[12] C. Lorenz *et al.*, "Multi-scale line segmentation with automatic estimation of width, contrast and tangential direction in 2D and 3D MEDICAL images," in *CVRMed-MRCAS 1997*, J. Troccaz, E. Grimson, and R. Mösges, Eds. Berlin, Germany: Springer, 1997, LNCS, pp. 233–242.

[13] Y. Sato *et al.*, "Three-dimensional multi-scale line filter for segmentation and visualization of curvilinear structures in medical images," *Med. Image Anal.*, vol. 2, no. 2, pp. 143–68, Jun. 1998.

[14] A. Frangi *et al.*, "Multiscale vessel enhancement filtering," in *MICCAI 1998*, W. M. Wells, A. C. F. Colchester, and S. L. Delp, Eds. Berlin, Germany: Springer, 1998, LNCS, pp. 130–137.

[15] K. Krissian *et al.*, "Model-based detection of tubular structures in 3D images," *Comput. Vis. Image Understand.*, vol. 80, no. 2, pp. 130–171, 2000.

[16] A. Vasilevskiy and K. Siddiqi, "Flux maximizing geometric flows," *IEEE Trans. Pattern Anal. Mach. Intell.*, vol. 24, no. 12, pp. 1565–1578, Dec. 2002.

[17] M. W. Law and A. C. Chung, "Efficient implementation for spherical flux computation and its application to vascular segmentation," *IEEE Trans. Image Process.*, vol. 18, no. 3, pp. 596–612, Mar. 2009.

[18] M. K. Law and A. S. Chung, "Three dimensional curvilinear structure detection using optimally oriented flux," in *Comput. Vision—ECCV 2008*, D. Forsyth, P. Torr, and A. Zisserman, Eds. Berlin, Germany: Springer, 2008, LNCS, pp. 368–382.

[19] S. J. Osher and J. A. Sethian, "Fronts propagating with curvature dependent speed: Algorithms based on Hamilton-Jacobi formulations," *J. Comput. Phys.*, vol. 79, pp. 12–49, 1988.

[20] L. M. Lorigo *et al.*, "CURVES: Curve evolution for vessel segmentation," *Med. Image Anal.*, vol. 5, no. 3, pp. 195–206, Sep. 2001.

[21] N. D. Forkert *et al.*, "3D cerebrovascular segmentation combining fuzzy vessel enhancement and level-sets with anisotropic energy weights," *Magn. Reson. Imag.*, vol. 31, no. 2, pp. 262–71, Feb. 2013.

[22] S. Beriault *et al.*, "Automatic trajectory planning of DBS neurosurgery from multi-modal MRI datasets," in *MICCAI 2011*, G. Fichtinger, A. L. Martel, and T. M. Peters, Eds. Berlin, Germany: Springer, 2011, LNCS, pp. 259–66.

[23] S. Beriault *et al.*, "A multi-modal approach to computer-assisted deep brain stimulation trajectory planning," *Int. J. Comput. Assist. Radiol. Surg.*, vol. 7, no. 5, pp. 687–704, Sep. 2012.

[24] S. Barnes, M. Barth, and P. Koopmans, "Automatic vein segmentation and lesion detection: From SWI-MIPs to MR venograms," in *Susceptibility Weighted Imaging in MRI*. New York: Wiley, 2011, pp. 605–618.

[25] P. J. Koopmans *et al.*, "MR venography of the human brain using susceptibility weighted imaging at very high field strength," *MAGMA*, vol. 21, no. 1-2, pp. 149–58, Mar. 2008.

[26] N. Vigneau-Roy *et al.*, "Regional variations in vascular density correlate with resting-state and task-evoked blood oxygen level-dependent signal amplitude," *Hum. Brain Mapp.*, vol. 35, no. 5, pp. 1906–20, May 2014.

[27] S. Z. Li, *Markov Random Field Modeling in Image Analysis*. New York: Springer, 2009.

[28] S. Bériault *et al.*, "Automatic Markov random field segmentation of susceptibility-weighted MR venography," in *CLIP 2013*, M. Erdt, M. G. Linguraru, and C. O. Laura, Eds. *et al.* Berlin, Germany: Springer, 2014, LNCS, pp. 39–47.

[29] Z. Karimaghaloo *et al.*, "Hierarchical Conditional random fields for detection of gad-enhancing lesions in multiple sclerosis," in *MICCAI 2012, Part II*, N. Ayache, H. Delingette, and P. Golland, Eds. *et al.* Berlin, Germany: Springer, 2012, LNCS, pp. 379–86.

[30] Z. Karimaghaloo *et al.*, "Automatic detection of gadolinium-enhancing multiple sclerosis lesions in brain MRI using Conditional random fields," *IEEE Trans. Med. Imag.*, vol. 31, no. 6, pp. 1181–94, Jun. 2012.

[31] J. Besag, "On the statistical-analysis of dirty pictures," *J. R. Stat. Soc. Ser. B-Methodol.*, vol. 48, no. 3, pp. 259–302, 1986.

[32] Y. Boykov and V. Kolmogorov, "An experimental comparison of min-cut/max-flow algorithms for energy minimization in vision," *IEEE Trans. Pattern Anal. Mach. Intell.*, vol. 26, no. 9, pp. 1124–1137, Sep. 2004.

[33] Y. Boykov, O. Veksler, and R. Zabih, "Fast approximate energy minimization via graph cuts," *IEEE Trans. Pattern Anal. Mach. Intell.*, vol. 23, no. 11, pp. 1222–1239, Nov. 2001.

[34] A. P. Dempster, N. M. Laird, and D. B. Rubin, "Maximum likelihood from incomplete data via the EM algorithm," *J. R. Stat. Soc. Ser. B (Methodol.)*, vol. 39, no. 1, pp. 1–38, 1977.

[35] L. Antiga, "Generalizing vesselness with respect to dimensionality and shape," *Insight J.*, 2007.

[36] D. Nain, A. Yezzi, and G. Turk, "Vessel segmentation using a shape driven flow," in *Medical Image Computing and Comput.-Assisted Intervention—MICCAI 2004*, C. Barillot, D. Haynor, and P. Hellier, Eds. Berlin, Germany: Springer, 2004, LNCS, pp. 51–59.

[37] C. Denk and A. Rauscher, "Susceptibility weighted imaging with multiple echoes," *J. Magn. Reson. Imag.*, vol. 31, no. 1, pp. 185–91, Jan. 2010.

[38] J. G. Sled, A. P. Zijdenbos, and A. C. Evans, "A nonparametric method for automatic correction of intensity nonuniformity in MRI data," *IEEE Trans. Med. Imag.*, vol. 17, no. 1, pp. 87–97, Feb. 1998.

[39] L. G. Nyul, J. K. Udupa, and Z. Xuan, "New variants of a method of MRI scale standardization," *IEEE Trans. Med. Imag.*, vol. 19, no. 2, pp. 143–150, Feb. 2000.

[40] S. F. Eskildsen *et al.*, "BEaST: Brain extraction based on nonlocal segmentation technique," *Neuroimage*, vol. 59, no. 3, pp. 2362–73, Feb. 2012.

[41] P. Coupe *et al.*, "An optimized blockwise nonlocal means denoising filter for 3-D magnetic resonance images," *IEEE Trans. Med. Imag.*, vol. 27, no. 4, pp. 425–41, Apr. 2008.

[42] N. Wiest-Daesslé *et al.*, "Rician noise removal by non-local means filtering for low signal-to-Noise ratio MRI: Applications to DT-MRI," in *MICCAI 2008*, D. Metaxas, L. Axel, and G. Fichtinger, Eds. *et al.* Berlin, Germany: Springer, 2008, LNCS, pp. 171–179.

[43] W. L. Nowinski *et al.*, "A 3D model of human cerebrovasculature derived from 3T magnetic resonance angiography," in *Neuroinformatics*. New York: Springer, 2009, vol. 7, pp. 23–36.

[44] L. R. Dice, "Measures of the amount of ecologic association between species," *Ecology*, vol. 26, no. 3, pp. 297–302, 1945.

[45] M. Descoteaux, D. L. Collins, and K. Siddiqi, "A geometric flow for segmenting vasculature in proton-density weighted MRI," *Med. Image Anal.*, vol. 12, no. 4, pp. 497–513, Aug. 2008.

[46] C. Sutton and A. Mccallum, "Piecewise training for structured prediction," *Mach. Learn.*, vol. 77, no. 2-3, pp. 165–194, 2009.

[47] Y. Rubner, C. Tomasi, and L. J. Guibas, "A metric for distributions with applications to image databases," in *Proc. 6th Int. Conf. Comput. Vis.*, 1998, pp. 59–66.

[48] P. A. Yushkevich *et al.*, "User-guided 3D active contour segmentation of anatomical structures: Significantly improved efficiency and reliability," *Neuroimage*, vol. 31, no. 3, pp. 1116–1128, Jul. 2006.

[49] B. Aubert-Broche *et al.*, "Twenty new digital brain phantoms for creation of validation image data bases," *IEEE Trans. Med. Imag.*, vol. 25, no. 11, pp. 1410–6, Nov. 2006.

[50] V. Fonov *et al.*, "Unbiased average ageappropriate atlases for pediatric studies," *Neuroimage*, vol. 54, no. 1, pp. 313–27, Jan. 2011.

[51] D. L. Collins *et al.*, "Automatic 3D model-based neuroanatomical segmentation," *Human Brain Mapp.*, vol. 3, pp. 190–208, 1995.